Bias-controlled plasmon switching in lithium-doped graphene on dielectric model Al2O3 substrate

Despoja, Vito; Jakovac, Josip; Golenić, Neven; Marušić, Leonardo

npj | 2D Materials and Applications

www.nature.com/npj2dmaterials

ARTICLE OPEN

Check for updates

Bias-controlled plasmon switching in lithium-doped graphene on dielectric model Al_2O_3 substrate

Vito Despoja[1,2]✉, Josip Jakovac[1], Neven Golenić[1,3] and Leonardo Marušić[4]

Graphene doped by lithium atoms supports a strong Dirac plasmon, a weak acoustic plasmon and a strong interband plasmon Li($\pi+\sigma$). Here we demonstrate that applying a positive or negative bias on the lithium-doped graphene causes the appearance ('switching ON') or disappearance ('switching OFF') of the Li($\pi+\sigma$) plasmon and the 'conversion' of the Dirac plasmon into a strong acoustic plasmon. This has two important consequences: 1. bias-controlled UV optical activity of the Li-doped graphene and 2. bias-controlled position of the 2D plasmon centroid. These effects turn out to be very robust and independent of the details of the experimental setup, which means that they should be easily experimentally verified, and very attractive for potential applications.

npj 2D Materials and Applications (2020)4:19 ; https://doi.org/10.1038/s41699-020-0151-1

INTRODUCTION

Experimental study of the crystal and electronic structure of single-layer graphene (SLG) on the Al_2O_3[1–5], SiO_2[6–8], or SiC[9–12] substrates obtained by chemical-vapor deposition (CVD) and/or exfoliation techniques is a widely explored methodology and becomes a routine. Moreover, in the recent years, various technologies, such as metal-free or metal-assisted graphene growth, have been developed. Using a metal-free method one can obtain a graphene film on insulated substrates directly, but so far only nanometer-scale graphene crystallites have been obtained, unless higher temperature[5] or longer process times[13] experiments were conducted. On the other hand, using a metal-assisted three-step method[14] the noble or transition metals surfaces (Cu, Ag, or Ir) can be used to obtain high-quality micrometer-scale graphene crystallites on insulating surfaces[15–17], such as e.g. syntheses of high-quality graphene on Al_2O_3(0001) surface assisted by Cu(111) surface.

The plasmonic properties of doped graphene on Al_2O_3, SiO_2, or SiC in infrared and THz frequency range (interesting for application) have been experimentally and theoretically widely explored[3,4,10–12,18–20]. These experimental studies show that graphene, when doped by electron donors or acceptors, supports a collective electronic mode called the Dirac plasmon (DP), which can be exploited in many plasmonics applications[21–30]. Graphene doped by alkali atoms, such as e.g. Li, Na, K, Cs on different metallic surfaces, such as e.g. Ir(111), Cu(111), and Ni(111) are extensively studied in many experimental or joined theoretical and experimental studies[31–37]. In these studies the most attention is paid to achieving self-standing (decoupled from the surface as much as possible) graphene with the lowest Moire corrugation. The plasmonic properties of the graphene epitaxial growth on metallic surfaces, such as Pt(111), Cu(111), or Ir(111) have been extensively studied[38–41], and it has been shown that the metallic surface abundantly donates electrons to the graphene π band so that it supports a strong DP, which modifies under the influence of strong metallic screening and becomes an acoustic plasmon, which authors also called 'sheet plasmon resonance'. The electron-energy-loss-spectra (EELS) measurements of the plasmon spectra on simple metallic surfaces[42] or in the alkali metal bilayers deposited on the Cu(111) or Ni(111) surfaces[43–45] showed a negative surface-plasmon dispersion but also evidence of a multipole surface plasmon. Very recently, the Dirac and acoustic plasmons in the lithium-doped and cesium-doped graphene on Ir (111) surfaces have also been studied theoretically[46].

All these studies show that the alkali-doped graphene (AC_x), where the electron or hole injection is achieved chemically, by means of electron donors or acceptors, offers some unexplored and exciting plasmonic properties which are not present in the electrostatically doped (biased) SLG, where the electron or hole injection is achieved by applying an external voltage to pristine graphene. In our recent theoretical investigations[47,48] we demonstrated that the alkali-doped graphenes LiC_2, LiC_6, CaC_6, and CsC_8 support very strong DP and sometimes (depending on the alkali atoms) a weak acoustic plasmon (AP). The mechanism of the formation of a strong DP is well known. Alkali atoms abundantly donate electrons to the graphene layer, its π band becomes heavily doped which causes a substantial increase of the effective number of the 'free' charge carriers (electrons) and thus the DP spectral weight. On the other hand the alkali atoms in AC_x usually form a superlattice, i.e. they metalize and form a parabolic σ band crossing the Fermi level. This band supports another plasmon which interacts with the DP in the graphene and becomes an acoustic like branch or AP[49–51]. The LiC_2 also supports an inter-band (intra-system) Li($\pi+\sigma$) plasmon which is built from transitions between parabolic occupied Li(σ) and unoccupied Li (π) bands in Γ point of the Brillouin zone (BZ). On the other hand, the LiC_6 supports an inter-band inter-system plasmon (IP) built from the interband transitions between C(π) and Li(σ) bands.

In order to provide an accurate description and capture all interesting plasmonic effects in the calculations, it is important to include the Coulomb screening coming from the adjacent substrate. Our recent theoretical studies[52] show that a strong Ir (111) screening completely destroys the AC_x plasmonics, so that e.g. in the cases of Li and Cs-doped graphene the DP is strongly suppressed, etc. Something similar applies to other metallic substrates such as Al(111), Au(111) or Cu(111). Therefore, in order to conserve all plasmonic properties of the alkali-doped graphene

[1]Institute of Physics, Bijenička 46, 10000 Zagreb, Croatia. [2]Donostia International Physics Center (DIPC), Paseo Manuel de Lardizabal 4, 20018 Donostia-San Sebastián, Spain. [3]Department of Physics, University of Zagreb, Bijenička 32, HR-10000 Zagreb, Croatia. [4]Maritime Department, University of Zadar, M. Pavlinovića 1, HR-23000 Zadar, Croatia. ✉email: vito@phy.hr

it is more appropriate to use wide band-gap semiconducting substrates, such as SiO_2, SiC, or Al_2O_3. Their frequency-independent dielectric functions (for $\omega < \Delta$, where Δ is the band-gap) just slightly red shift the 2D plasmon energy and just slightly reduce the plasmon oscillator strength.

In this paper, we investigate the intensity of the 2D plasmons in lithium-doped graphenes LiC_x; $x = 2$, 6 deposited on the Al_2O_3 surface, where special attention is paid to exploring how the additional hole or electron injection, achieved through electrostatic bias, influences the interplay between the intra-band DP and the intra-band AP (or an inter-band plasmon IP), and 'switches ON or OFF' the interband Li($\pi + \sigma$) plasmon. We show that if the holes are injected in the LiC_2 or in the LiC_6 the weak Landau-damped DP will be converted into a strong AP or IP, respectively. The hole injection also causes the appearance ('switching ON') and disappearance ('switching OFF') of the Li($\pi + \sigma$) plasmon in LiC_2 and LiC_6, respectively. Moreover, for larger wave vectors Q the injection of electrons in LiC_6 causes the appearance ('switching ON') of the Li($\pi + \sigma$) plasmon. Both systems support a strong long wavelength DP which does not exist in the electrostatically doped SLG (here and throughout the paper the acronym SLG is used exclusively for the chemically undoped single layer graphene). The diversity of these extraordinary plasmonic properties can be very useful for plasmonic applications and should be easily verified experimentally.

In section "Methods", we present the method used to calculate the effective 2D dielectric function $\epsilon(\mathbf{Q}, \omega)$ of the LiC_x/Al_2O_3 composite. In section "Results" we present the results for the EELS $\sim -\Im[1/\epsilon]$ in the LiC_2/Al_2O_3 and LiC_6/Al_2O_3 composites, and the influence of the electrostatic bias to these spectra. To demonstrate how interesting these results are, we compare them with the spectra in the electrostatically biased SLG, where these effects do not appear at all. Finally, we emphasize the effects which could be interesting for plasmonic applications.

RESULTS

LiC_2/Al_2O_3 composite

The systems we study consist of graphene doped by lithium atoms LiC_x deposited on an Al_2O_3 surface (the LiC_x/Al_2O_3 composite), as shown in Fig. 1. The graphene layer is in the $z = 0$ plane, and is located at the distance $h = 3.2$ Å^2 from the Al_2O_3 surface. The alkali atoms adlayer is in the $z = d$ plane. Figure 2a and c shows the projected band structures of the LiC_2 and LiC_6, respectively. For comparison, Fig. 2b and d shows projected band structures of the LiC_2/Al_2O_3 and LiC_6/Al_2O_3 composites, respectively. The orange color denotes the bands with the predominant C,Li(π) character, while the magenta color denotes the bands with the predominant Li(σ) character.

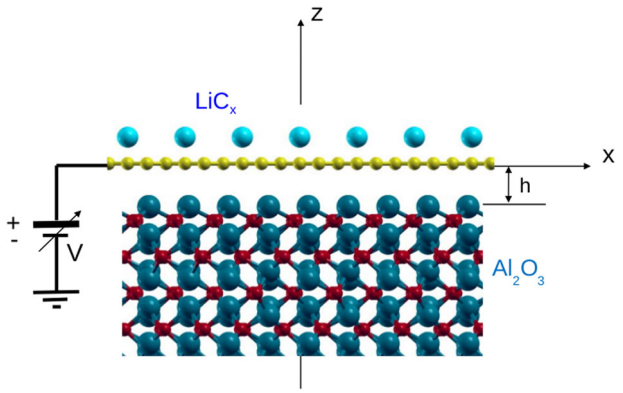

Fig. 1 Crystal structure of alkali-doped graphene on Al_2O_3 surface or LiC_x/Al_2O_3 composite. The doped graphene is connected to a tunable bias V.

A large van der Waals equilibrium separation h results in a small electronic overlap between the LiC_x slab and the Al_2O_3 surface which enables us to calculate the dynamically screened Coulomb interaction of LiC_x/Al_2O_3 composite by combining the LiC_x non-interacting electrons response function $\chi^0_{LiC_x}$ and Al_2O_3 macroscopic dielectric function ϵ_S, as will be explained below. This considerably reduces the unit cell size and significantly saves the computational time and memory requirements. This will be especially useful when studying the dynamical response in LiC_x/Al_2O_3 composite for different biases $V \neq 0$ or $E_F \neq 0$.

We show the EELS intensities in lithium-doped graphene LiC_2 and LiC_6 for various electrostatic biases and for two different wave vectors Q. In order to demonstrate the robustness and diversity of the extraordinary plasmonic properties in chemically doped graphene LiC_x, we compare them with the EELS intensities in the equivalently electrostatically biased SLG. All 2D structures are deposited on Al_2O_3 surface, as shown in Fig. 1. It should be noted that we have chosen for the alkali atoms to be adsorbed on the graphene and the wide band-gap semiconducting Al_2O_3 surface to be used as the substrate. This choice is important, because when the alkali atoms are intercalated between the graphene layer and the metallic substrate, as shown in ref. [46] where LiC_2 or CsC_8 are at the equilibrium separation h from the Ir(111) surface, the substrate destroys the DP and AP, although even a small displacement from the equilibrium position causes both plasmons to recover. This is what motivated us to use the semiconducting surface instead of a metallic one (in order to avoid strong metallic screening which destroys the DP) and to adsorb rather than intercalate the alkali atoms (in order to protect the Li(σ) band which supports the AP). This enables both the AP and DP to survive for the realistic equilibrium LiC_x/Al_2O_3 distances. Moreover the only effect of the insulating surface is that it slightly red shifts the 2D plasmon energy and slightly reduces the plasmon oscillator strength in comparison with the self-standing case. In other words, changing the height h only slightly influences the plasmon properties. This was verified computationally but is not presented here. Figure 3a and b shows the EELS intensities in LiC_2/Al_2O_3 composite for wave vectors $Q = 0.054$ a.u. and $Q = 0.148$ a.u., respectively, as functions of the Fermi energy E_F (modified by the electrostatic bias). Our energy scale is set so that the Fermi level of the unbiased composite is $E_F = 0$, so $E_F < 0$ or $E_F > 0$ means that the holes or electrons are injected in the sample, respectively. The upper (red) scale at the abscissa shows the Fermi energy with respect to the graphene Dirac point, e.g. the Fermi energy of the unbiased LiC_2, with respect to the Dirac point, is $E_F = 1.78$ eV (also shown by the vertical lines in the figure). The horizontal line ($v_F^\pi Q$) denotes the upper edge of C(π) intra-band and the sloped line ($2E_F - v_F^\pi Q$) denotes the lower edge of the C(π) inter-band electron–hole continuum in the Dirac cone approximation. Figure 3a shows that the unbiased LiC_2 supports a very weak AP, very strong DP, and just emerging (for the wave vector $Q = 0.054$ a.u.) Li($\pi + \sigma$) plasmon. The AP and DP are intra-band plasmons built from the intraband transitions within C(π) and Li(σ) bands crossing the Fermi level, as shown in Fig. 2a and b. Li($\pi + \sigma$) is an interband plasmon built from the transitions between the parabolic Li(σ) and Li(π) bands around the Γ point, as denoted in Fig. 2a and b. If we inject extra electrons in the system ($E_F > 0$) the number of the effective charge carriers increases so the DP frequency and intensity increases, while the AP and Li($\pi + \sigma$) plasmon remain weak. It is important to note that the DP intensity is greatly enhanced and it becomes the dominant mode in the entire spectra. On the other hand, as can be seen in Fig. 3e, the DP in SLG for the equivalent bias ($E_F > 1.78$ eV) does not even exist. For the larger wave vector $Q = 0.148$ a.u., as shown in Fig. 3b, the unbiased ($E_F = 0$) LiC_2 supports a very strong Li($\pi + \sigma$) plasmon, weaker (Landau damped) DP and weak AP. If we inject extra

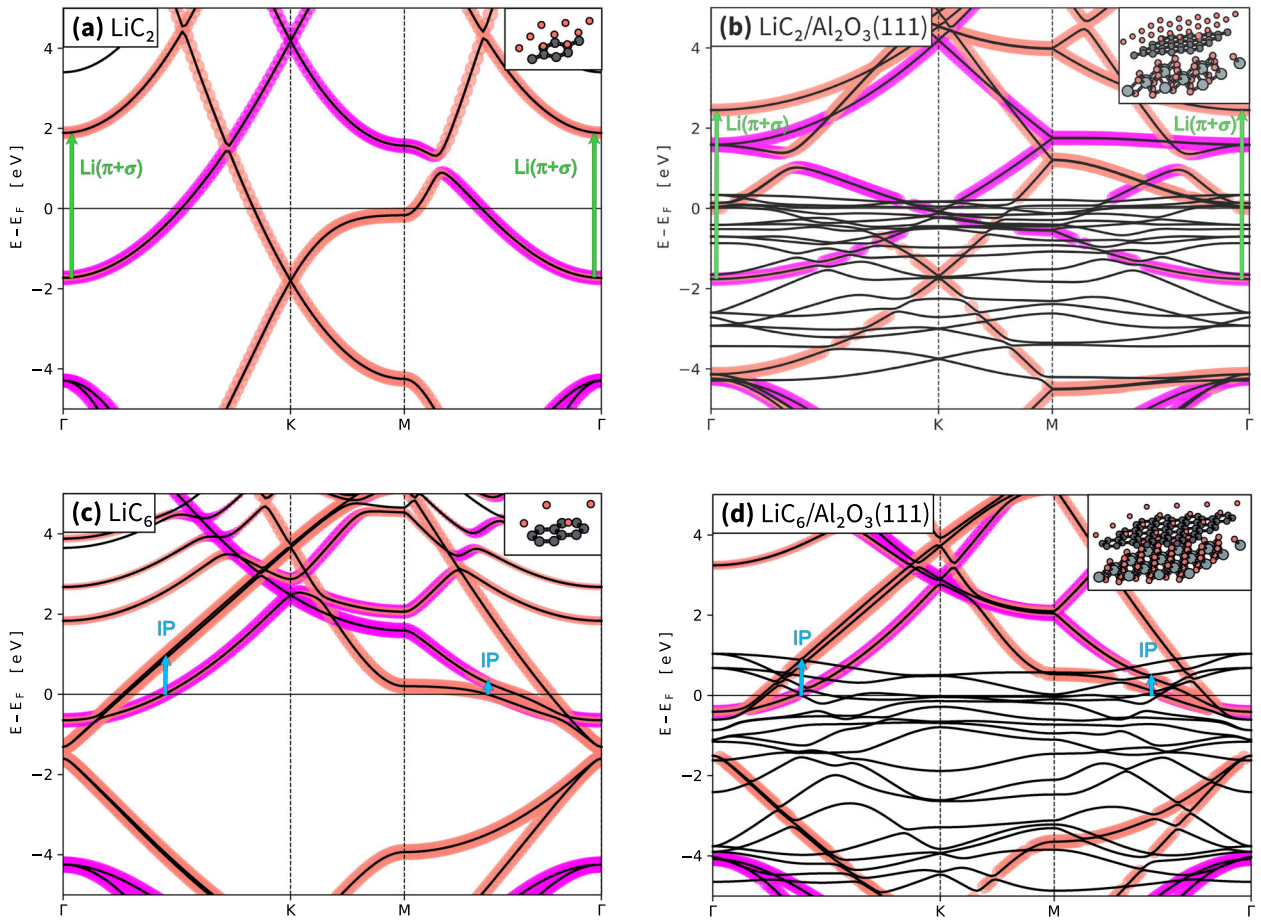

Fig. 2 The projected band structure in (**a**) LiC_2, (**b**) LiC_2/Al_2O_3, (**c**) LiC_6, and (**d**) LiC_6/Al_2O_3 composites. The orange color denotes the bands with C,Li(π) character and the magenta color denotes the bands with Li(σ) character.

electrons in the system ($E_F > 0$) the Li($\pi + \sigma$) plasmon for ($E_F \approx$ 0.25 eV) becomes even sharper and a more intensive collective mode. The DP frequency and intensity increases following the same pattern as in the SLG shown in Fig. 3f. We can also see that the DP in SLG is more intensive.

However, when holes are injected in the system ($E_F < 0$) some extraordinary effects occur. In addition to the expected fast decrease of the energy and intensity of the DP, for $E_F < -0.5$ eV we can notice the significant increase of the Li($\pi + \sigma$) plasmon intensity, or 'switching ON' of the Li($\pi + \sigma$) plasmon. On the other hand, as shown in Fig. 3e, at similar frequencies the SLG supports just a broad π plasmon, with frequency independent of the bias. For large hole doping ($E_F < -1$ eV) the strong DP approaches the weak AP (with frequency almost independent of the bias), and at $E_F \approx -1.3$ eV these two modes overlap and hybridize, leading to the avoided crossing. We can see that with the increase of the hole injection the DP intensity weakens, while the AP intensity increases, so the AP assumes the role of the DP, and its frequency becomes dependent on the bias until it reaches $\omega = 0$.

This effect is even more evident for the larger wave vector $Q =$ 0.148 a.u., shown in Fig. 3b. As the hole injection increases the DP frequency and intensity decreases, almost the same way it does in the chemically intrinsic graphene, shown in Fig. 3f. For any hole injection the DP is Landau damped by the C(π) inter-band electron–hole excitations (since it is above the $2E_F - v_F^{\pi}Q$ line) but for the hole injection $E_F < -1.2$ eV it enters the C(π) intra-band continuum $v_F^{\pi}Q$. Again, for weak hole injection the AP frequency barely depends on the bias, but for stronger hole injection the AP intensity increases while the DP intensity decreases and its frequency approaches the AP frequency. Finally, for $E_F \approx -0.75$ eV we have the hybridization leading to the avoided crossing and the AP takes over. It becomes a well-defined collective mode and its frequency decreases with the increase of the hole injection, until it reaches $\omega = 0$. For $E_F < -0.75$ eV, contrary to the DP, the AP is below the $v_F^{\pi}Q$ line and above the $2E_F - v_F^{\pi}Q$ line, which means that it is completely immersed in the C(π) intra-band and inter-band electron–hole continuum. However, due to its Li(σ) character it remains a sharp and undamped plasmon mode.

The Li($\pi + \sigma$) plasmon also shows interesting behavior, which could be very interesting for potential applications in the UV frequency range. Namely, already for the light hole injection $E_F \leq -0.25$ eV the Li($\pi + \sigma$) intensity considerably increases so that its oscillatory strength becomes an order of magnitude larger than the Landau-damped DP (as also shown in Fig. 4b). The Li($\pi + \sigma$) remains strong well-defined interband plasmon as the hole injection increases, until it reaches $E_F \approx -1.2$ eV when the plasmon intensity rapidly drops to zero. This interplay between the AP and the DP and the appearance of the strong Li($\pi + \sigma$) plasmon, of course, does not occur in chemically undoped graphene, as can be seen in Fig. 3f.

This is even more evident from Fig. 4, which show the evolution of EELS in the LiC_2/Al_2O_3 composite as a function of the increasing hole injection (positive bias) for the transfer wave vector, $Q =$ 0.148 a.u. Figure 4a shows the unbiased sample ($E_F = 0$) and the three plasmons we already described: a weak AP, a somewhat stronger DP, and a very strong Li($\pi + \sigma$) plasmon, and Fig. 4b–h show how these plasmons change as we inject the holes in the system. Figure 4 also shows (magenta line) the real part of the

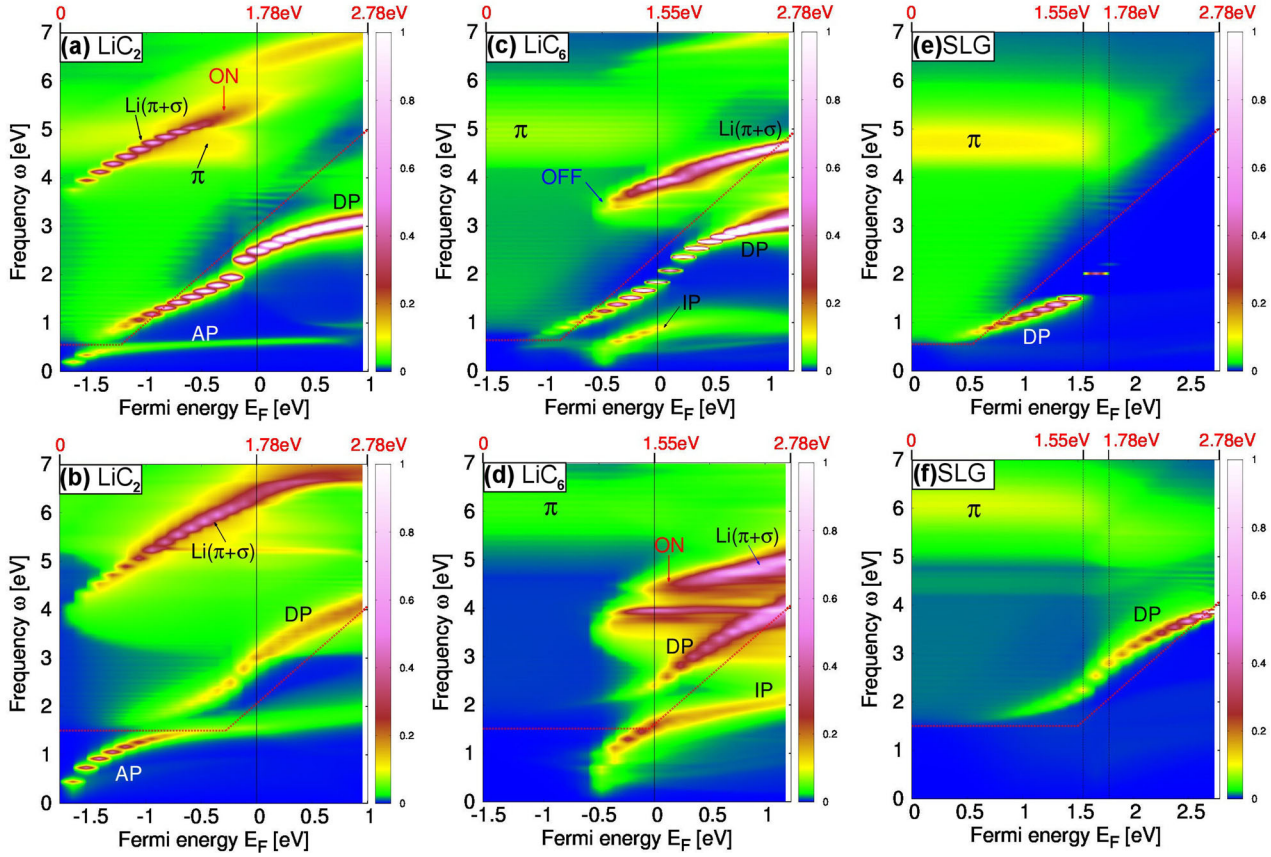

Fig. 3 The EELS intensities in the LiC_2/Al_2O_3 composite as function of the Fermi energy (EF) for (**a**) Q = 0.054 a.u. and (**b**) for Q = 0.148 a.u. The EELS intensities in the LiC_6/Al_2O_3 composite for (**c**) Q = 0.063 a.u. and (**d**) for Q = 0.149 a.u. The EELS intensities in SLG/Al2O3 composite for (**e**) Q = 0.054 a.u. and (**f**) for Q = 0.148 a.u. The upper (red) scale at the abscissa shows the Fermi energy relative to the graphene Dirac point. The vertical lines denote the Fermi energies in the LiC_6 ($E_F^{LiC_6} = 1.55$ eV) and LiC_2 ($E_F^{LiC_2} = 1.78$ eV) relative to the graphene Dirac point. The horizontal lines ($v_F^{\pi}Q$) denote the upper edge of the C(π) intra-band and the sloped lines ($2E_F - v_F^{\pi}Q$) denote the lower edge of the C(π) inter-band electron–hole continuum in the Dirac cone approximation.

effective 2D dielectric function ($\Re\epsilon$). In Fig. 4a we can see that the $\Re\epsilon$ has 'kinks' at the DP and AP frequencies, but it does not have a zero. On the other hand the $\Re\epsilon$ has a zero exactly at the Li ($\pi+\sigma$) peak which means that it is a well-defined collective mode (plasmon). In the unbiased system the Li($\pi+\sigma$) plasmon is still broad and dispersive, however, Fig. 4b shows that already for small hole injection ($E_F = -0.24$ eV) it becomes a sharp plasmon, slightly red shifted. Figure 4c and d shows that with the further hole injection the Li($\pi+\sigma$) plasmon becomes sharper and more red shifted. This phenomenon can be explained by observing the band structure in Fig. 2a, b. As the hole injection increases (i.e. the Fermi level decreases) the part of the Li(σ) parabolic band below the Fermi level becomes more similar to the part of the Li(π) parabolic band exactly above it. This means that for the larger biases all the occupied Li(σ) states can be almost perfectly transferred into the unoccupied Li(π) states. In other words, this causes coherent electron–hole transitions from the parabolic Li(σ) band into the parabolic Li(π) band and finally a well-defined collective mode, with energy higher than the energy of the single-particle Li(σ) → Li(π) electron–hole transitions. Also, Fig. 4a–d clearly shows that the DP intensity and energy decrease with the increase of the hole injection, as expected. However, we also see something quite unexpected: as the DP intensity decreases the AP intensity increases and the mode is weakly red shifted. This phenomenon becomes especially intriguing for stronger bias.

Figure 4e–h shows EELS in LiC_2/Al_2O_3 composite for the electrostatic bias in the interval $E_F = -0.96$ to -1.67 eV, as denoted in the figures. We can seen that, contrary to the case in Fig. 4a–d already for $E_F = -0.96$, shown in Fig. 4e, the $\Re\epsilon$ starts has a zero at the AP. This classifies the AP as a well-defined collective mode, and in EELS it also appears as a sharp, well-defined peak. This becomes especially noticeable in Fig. 4f, g, showing the EELS for $E_F = -1.19$ eV and $E_F = -1.43$ eV, respectively. The AP takes over the entire spectral weight of the low-energy EELS and it behaves almost as an ideal bosonic mode (or ideal harmonic oscillator) with $\Re\epsilon \sim 2\omega_{AP}/(\omega^2 - \omega_{AP}^2)$ and $\Im\frac{1}{\epsilon} \sim \delta(\omega - \omega_{AP})$, where ω_{AP} is the AP frequency. For even larger bias, $E_F = -1.67$ eV, although the $\Re\epsilon$ still has a zero at the AP peak, and the AP is still a well-defined bosonic mode, the AP intensity starts to decrease. This is because the AP is mostly built from the transitions within the Li(σ) band, and for bias this large the Fermi energy is already very close to the bottom of that band, as can be seen at the Γ point in Fig. 2a, b. As a result of this, the number of the charge carriers involved in the formation of the AP becomes drastically reduced and the AP oscillator strength weakens. As already mentioned, for larger hole injections the AP frequency changes towards $\omega = 0$. Figure 4e–h also show that for the larger biases the $\Re\epsilon$ still has a zero at Li($\pi+\sigma$) plasmon peak, which means that it remains a well-defined collective mode. Moreover, the Li($\pi+\sigma$) plasmon intensity rapidly decreases with the hole injection, even faster than the AP, although the reason is the same: the Li(σ) band gets less populated and consequently there are less available electrons which can be excited into the unoccupied Li(π) band.

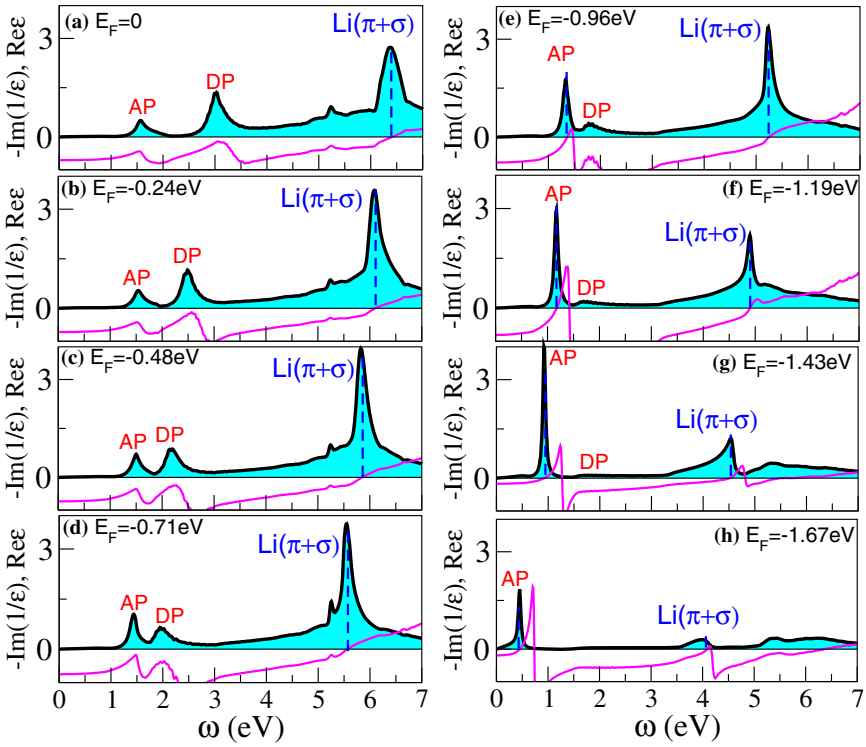

Fig. 4 EELS and $\Re\epsilon$ in LiC_2/Al_2O_3 composite for different positive biases ($E_F < 0$). The transfer wave vector is $Q = 0.148$ a.u.

LiC_6/Al_2O_3 composite

In order to demonstrate that the interesting plasmonic properties are not limited to specific Li atoms coverage, in Fig. 3c, d we show the EELS intensities in the LiC_6/Al_2O_3 composite for $Q = 0.063$ a.u. and $Q = 0.149$ a.u., respectively. We can see that for for $Q = 0.063$ a.u. the unbiased sample ($E_F = 0$) also supports a strong DP and a much stronger (and red shifted in comparison with LiC_2) Li $(\pi + \sigma)$ plasmon. Also at about $\omega \approx 0.8$ eV we can see the so-called interband plasmon (IP) which originates from the interband transitions between the C(π) and the Li(σ) bands, as indicated in Fig. 2c, d. This means that, contrary to the interband Li$(\pi + \sigma)$ plasmon, the IP is an inter-system plasmon and represents the charge density oscillations between the graphene and the Li adlayer, perpendicular to the LiC_6 surface[48]. As we increase the hole or electron injection the DP behaves almost the same as in the LiC_2. We can see that the Li$(\pi + \sigma)$ plasmon in the LiC_6 exists mostly for electron injection (opposite from the LiC_2), where it develops in a very intensive plasmon, comparable with the DP. However, already for a small hole injection ($E_F < -0.4$ eV) the Li$(\pi + \sigma)$ plasmon suddenly disappears. Figure 2c, d show us that this happens because in this case the parabolic Li(σ) is much closer to the Fermi level of the unbiased system, and as the Fermi level is shifted to $E_F < -0.4$ eV, the band becomes empty, so there are no more charge carriers to participate in the formation of Li$(\pi + \sigma)$ plasmon. This enables the 'switching OFF' of the very strong Li$(\pi + \sigma)$ plasmon by a small negative bias. This phenomenon, although in the opposite direction, occurs in the LiC_2, where small positive bias 'switches ON' the Li$(\pi + \sigma)$ plasmon, as demonstrated in Fig. 5. The IP is weaker but exists for all shown electron injections ($E_F > 0$). For the hole injection ($E_F < 0$) it slightly strengthens and for ($E_F < -0.4$) its frequency decreases and it suddenly disappears. We need to point out something very interesting: the unbiased LiC_6 (similar to the unbiased LiC_2) supports very strong DP which, together with the Li$(\pi + \sigma)$ for reasonable small electron injection becomes the dominant collective mode in the entire EELS. This is completely opposite

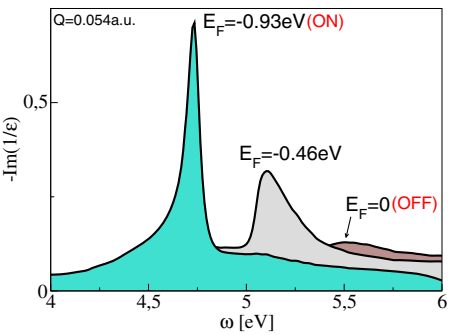

Fig. 5 Intensity of Li$(\pi + \sigma)$ plasmon in LiC_2/Al_2O_3 composite for three different hole dopings. The transfer wave vector is $Q = 0.054$ a.u.

to SLG which does not support any collective modes for the equivalent electrostatic biases, as can be seen in Fig. 3e.

For the larger wave vector $Q = 0.149$ a.u. shown in Fig. 3d and the electron injection ($E_F > 0$) the LiC_6 supports a DP substantially stronger than the DP in the LiC_2 or in the SLG. This is unusual considering that the DP is here also above $2E_F - v_F^{\pi}Q$ line, i.e. it is immersed in the inter-band C(π) electron–hole continuum. The Li $(\pi + \sigma)$ plasmon does not exist for the hole injection ($E_F < 0$), for the unbiased sample ($E_F = 0$) it is broad and weak, and for the electron injection ($E_F > 0$) it suddenly develops in a broad but strong plasmon mode. We can notice that even a very small electron injection ($E_F > 0.25$ eV) causes the 'switching ON' of the Li $(\pi + \sigma)$ plasmon. The IP is blue shifted and much stronger than the IP for the smaller wave vector Q. For a small hole injection ($-0.3 < E_F < 0$ eV) the IP is very strong and for larger hole injection ($E_F < -0.4$ eV) its frequency decreases toward $\omega = 0$ until the mode suddenly disappears. For the electron injection ($E_F > 0$) the IP's frequency barely depends on the bias but the mode remains substantially strong and well defined. We can notice that the IP in LiC_6 in many ways mimics the AP in the LiC_2. It is the plasmon with

the lowest energy, for the hole injection it is strong and its frequency strongly depends on the bias, while for the electron injection it is weaker and its frequency weakly depends on the bias. As the DP weakens, the IP strengthens, and finally the DP–IP avoided crossing is noticeable. Actually, this correspondence is very unusual, considering that the IP is an inter-system and inter-band plasmon while the AP is an intra-system and intra-band plasmon.

For the hole injection ($E_F < 0$), the LiC_6 also supports a very broad π plasmon, weaker but similar to the one in the SLG, shown in Fig. 3e and f. For the electron injection, especially when the Fermi energy is above the van Hove singularity at M point (which corresponds to $E_F > 1.8$ eV with respect to the Dirac point) the π plasmon disappears. This is especially obvious in Fig. 3e. The LiC_2 does not support the π plasmon but just some remains of this mode which can be noticed in Fig. 3a.

Finally, we need to emphasize that the LiC_6 supports two very intensive interband plasmons; 1. the already described IP which is mainly in the IR frequency range $0.6 < \omega < 1.5$ eV and 2. the Li($\pi + \sigma$) plasmon which is in the UV $3 < \omega < 6$ eV frequency range. Frequency and intensity of either mode can be easily manipulated by injecting the electrons or holes in the sample which can be very attractive from the aspect of their applications. For example, Fig. 3c shows that small hole injection in the LiC_6 causes the 'switching OFF' of the Li($\pi + \sigma$) plasmon, and Fig. 3d shows that small electron injection causes the 'switching ON' of the Li($\pi + \sigma$) plasmon. Moreover, Fig. 3d suggests that small hole injection can be used to 'switch OFF' the IP plasmon which exists in the unbiased system.

DISCUSSION

We need to emphasize that Figs. 4 and 5 show two very interesting physical phenomena which are experimentally feasible and could be very useful in plasmonic application.

1. Light hole injection ($E_F < -0.3$ eV) of the LiC_2/Al_2O_3 system causes the appearance of a strong Li($\pi + \sigma$) plasmon with a frequency in the UV range. As can be seen in Figs. 5 and 3a this effect is especially pronounced for smaller wave vectors $Q = 0.054$ a.u. when a small increase of the hole injection causes the appearance (or 'switching ON') of the Li($\pi + \sigma$) plasmon. On the other hand, as shown in Fig. 3c, quite the opposite occurs in the LiC_6 where a small hole injection causes the disappearance (or 'switching OFF') of the strong Li($\pi + \sigma$) plasmon.
2. Heavier hole injection ($E_F < -0.9$ eV) of the LiC_2/Al_2O_3 system causes the AP to become extraordinarily strong, taking the role of the DP which gets completely suppressed. This is nicely demonstrated in Fig. 6 showing the interplay between the DP and AP plasmons in LiC_2/Al_2O_3 composite for three different biases. Applicational aspect of this effect is moving the plasmon oscillations from the graphene layer to the Li add-layer and vice-versa. Namely, the DP represents the in-plane charge-density oscillations predominantly localized within the graphene layer, while the AP represents the in-plane charge density oscillations which are predominantly localized within the Li add-layer[47]. This means that the plasmon can be moved from one to another crystal plane by changing the bias, as denoted in Fig. 6.

The weakening of the DP is not surprising. As shown in Fig. 3b and f, and already explained, for the hole injection $E_F < -0.9$ eV (or $E_F < 0.88$ eV in SLG) the DP is far above the inter-band line $\omega = 2E_F - v_F^{\pi}Q$ and it approaches the intraband line $v_F^{\pi}Q$ which means that the DP is strongly damped by the C(π) intra-band and inter-band electron–hole excitations. However, the question why the AP intensity increases with the hole injection is very intriguing? The answer is the screening of the AP by the approaching DP.

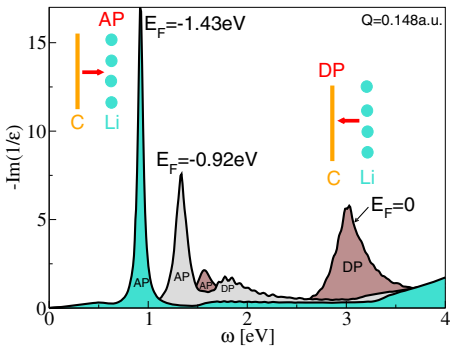

Fig. 6 Interplay between DP and AP in LiC_2/Al_2O_3 composite for three different hole dopings. The transfer wave vector is $Q = 0.148$ a.u.

Figure 3a and b shows that, while the DP and the AP are far away, the AP's frequency barely changes as a function of bias. However, as the hole injection is increased, the DP (with the frequency highly dependent of the bias) reaches the AP, and the already described avoided crossing occurs. This means that AP and DP strongly interact exchanging their symmetry and other properties. The crucial consequence of this interaction is that for high hole doping the $\Re\epsilon$ has a zero the AP (see Fig. 4e), meaning that all the available 'free' charge carriers are employed in the formation of the collective mode, which results in the strong AP peak. The question is also why the AP is not damped by the C(π) intra-band and inter-band electron–hole excitations, even though for $E_F < -1.0$ eV its frequency is $\omega_{AP} < 1.5$ eV, which means that it is immersed in the continuum of these excitations (see Fig. 3b). This is due to the symmetry reason, since the AP has Li(σ) intra-band character and it weakly interacts with the C(π) electron–hole excitations.

We demonstrated that the chemically doped graphenes LiC_x/Al_2O_3; $x = 2$, 6 support plasmons, such as the Li($\pi + \sigma$) plasmon or AP, which do not exist in chemically undoped graphene (SLG). It is especially important that these plasmons can be easily manipulated by injecting extra electrons or holes in the sample by applying a bias voltage. For example, by changing the electron or hole injection of the LiC_x/Al_2O_3 sample the Li($\pi + \sigma$) plasmon can be 'switched ON' or 'OFF' or the DP can be 'converted' into the AP (or the IP in the LiC_6), and vice versa. The plasmonic properties of LiC_x/Al_2O_3 composites for the electron ($E_F > 0$) and hole ($E_F < 0$) injections and for different wave vectors Q are highlighted in Table 1.

Finally, the crucial property of the composites studies in this paper is the robustness of these extraordinary plasmonic properties. The results presented in this paper, combined with some additional calculations, not presented here, show that the 'switching' and 'conversion' effects do not depend on the choice of the substrate, the concentration of the chemical doping, or the choice of the alkali atom used as the dopant. Also the effects do not depend on the relative position of the alkali addlayer, i.e. they will not significantly change if the alkali atoms were intercalated (between graphene and the substrate) instead of being deposited on the graphene layer. This means that these effects should be easily measurable without too much attention on the preparation of the sample.

METHODS

Calculation of the effective 2D dielectric function

To calculate the Kohn–Sham (KS) wave functions $\phi_{n\mathbf{k}}$ and energy levels $E_n(\mathbf{k})$, i.e. the band structure, of LiC_x, $x = 2$, 6 slabs and bulk Al_2O_3 crystal we use the plane-wave self-consistent field DFT code (PWSCF) within the QUANTUM ESPRESSO (QE) package[53]. The core–electrons interaction is

Table 1. Overview of the plasmonic effects in the LiC_x/Al_2O_3 samples.

Sample	LiC_2/Al_2O_3		LiC_6/Al_2O_3	
Wave vector	$Q < 0.1$	$Q > 0.1$	$Q < 0.1$	$Q > 0.1$
Hole injection ($E_F < 0$)	Li($\pi + \sigma$) 'ON'	DP → AP	Li($\pi + \sigma$) 'OFF'	DP → IP
Electron injection ($E_F > 0$)	DP*		DP*	Li($\pi + \sigma$) 'ON'

DP* denotes very strong DP which does not exist in chemically undoped graphene (SLG).

approximated by the norm-conserving pseudopotentials[54]. The XC potential in the LiC_x is approximated by the Perdew–Zunger local density approximation (LDA)[55], and in the Al_2O_3 by the Perdew–Burke–Ernzerhof generalized gradient approximation (GGA)[56]. The ground state electronic densities for LiC_2, LiC_6, and Al_2O_3 are calculated using the $12\times12\times1$, $9\times9\times1$, and $9\times9\times3$ Monkhorst–Pack[57] K-point mesh sampling of the first BZ, respectively. For all systems the plane-wave cut-off energy is chosen to be 60 Ry (816 eV).

With respect to graphene, LiC_2 and LiC_6 form a 1×1 and $\sqrt{3}\times\sqrt{3}$ 2D hexagonal Bravais lattice with the unit cell constant $a = 4.65$ a.u. and $a = 8.056$ a.u.[58], respectively. The repeating LiC_x slabs are separated by $c = 23.3$ a.u. (12.3 Å). The equilibrium separations between the Li and graphene layers are $d = 4.1$ a.u. (2.17 Å) and 3.29 a.u. (1.74 Å), respectively[31,59]. For the Al_2O_3 we used the hexagonal Bravais lattice (12 Al and 18 O atoms in unit cell) with lattice constants $a = 9.0$ a.u. and $c = 24.55$ a.u.

The non-interacting electrons response functions of AC_x slabs $\chi^0_{AC_x}$ and the response function of the bulk Al_2O_3 crystal χ^0_S are calculated using a denser k-point mesh and more unoccupied bands. The $\chi^0_{LiC_2}$, $\chi^0_{LiC_6}$, and χ^0_S are calculated using $201\times201\times1$, $115\times115\times1$, and $21\times21\times7$ k-point meshes and the band summations are performed over 30, 50, and 120 bands, respectively. In the $\chi^0_{LiC_2}$ and $\chi^0_{LiC_6}$ calculation the damping parameter is $\eta = 20$ meV and in χ^0_S calculation $\eta = 100$ meV.

Even though the transfer wave vectors in the direction parallel to the slabs $\mathbf{Q} = (q_x, q_y, 0)$ considered in this investigation satisfy the condition $Q = |\mathbf{Q}| << 2\pi/a$ the crystal local field effects should be carefully treated. Namely, the strong dispersivity of the LiC_x dielectric response in the perpendicular direction (z) requires the inclusion of the crystal local field effects in the z direction. This means that LiC_x response functions are nonlocal in the perpendicular direction and can be Fourier transformed as $\chi(z,z') = \frac{1}{L}\sum_{G_z G_z'} e^{iG_z z - iG_z' z'} \chi_{G_z G_z'}$, where $\mathbf{G} = (\mathbf{G}_\parallel, G_z)$ are the reciprocal space vectors. The crystal local field energy cut off is 10 Ry (136 eV), which corresponds with $23G_z$ wave vectors. The dielectric response of the bulk Al_2O_3 crystal is calculated in an optical limit, i.e. the crystal local field energy cut-off is set to be zero.

The dynamically screened Coulomb interaction in the AC_x slabs can be calculated by solving the Dyson equation $w = v + v \otimes \chi^0_{AC_x} \otimes w$, where $v = \frac{2\pi}{Q} e^{-Q|z-z'|}$ is the bare Coulomb interaction[60], and $\otimes \equiv \int_{-c/2}^{c/2} dz$. The interaction between the charge density fluctuation at $z > -h$ and the charge density fluctuation at $z' > -h$ in the vicinity of a polarizable Al_2O_3 surface is mediated by the surface screened Coulomb interaction w_S instead of the bare Coulomb interaction v, where

$$w_S = v + D_S e^{-Q(z+z'+2h)}.$$

Here $D_S = (2\pi/Q)(1-\epsilon_S)/(1+\epsilon_S)$ is the Al_2O_3 surface response function ($\epsilon_S = \lim_{\mathbf{q}\to0}[1 - \frac{4\pi}{|\mathbf{q}|^2}\chi_S]$ is the Al_2O_3 macroscopic dielectric function, where $\mathbf{q} = (q_x, q_y, q_z)$ is the 3D transfer wave vector). When the LiC_x is deposited on the polarizable Al_2O_3 surface, and the replacement $v \to w_S$ is made, the dynamically screened Coulomb interaction of the entire AC_x/Al_2O_3 composite is obtained by solving the 'screened' Dyson equation:

$$w = w_S + w_S \otimes \chi^0_{LiC_x} \otimes w. \quad (1)$$

The effective 2D dielectric function can then be defined as

$$\epsilon^{-1}(\mathbf{Q},\omega) = w(\mathbf{Q},\omega, z=0, z'=0)/v_Q,$$

where $v_Q = \frac{2\pi}{Q}$, and finally the EELS is calculated as $S(\mathbf{Q},\omega) = -\frac{1}{\pi}\Im\epsilon^{-1}(\mathbf{Q},\omega)$.

The validity of the model

Efficient extensive investigation of the doping-dependent plasmonics in LiC_x/Al_2O_3 composites heavily depend on two very rigorous approximations:

Table 2. The injected charge ΔQ_{TOT}, the relative change of the lattice constant $\Delta a/a$, and the change of the Li–C separation (with respect to the RBA) Δd in the self-standing LiC_2 and LiC_6.

System	LiC_2		LiC_6	
RBA shift [eV]	−0.5	0.5	−0.5	0.5
ΔQ_{TOT} [e/u.c.]	−0.44	0.4	− 0.77	1.06
$\Delta a/a$	0.1%	2.4%	−1.4%	−0.1%
Δd [Å]	0	−0.48	0.12	0.002

1. Rigid bands approximation (RBA), where we 'freeze' the band structure and the charging of the system is simulated by shifting the Fermi level. This allows us to calculate the band structure of LiC_x only once which significantly simplifies the calculation.
2. Van der Waals limit, where we assume that the LiC_x and Al_2O_3 interact only via the long-range fluctuation–fluctuation Coulomb interaction and the band structure is weakly affected by the Al_2O_3 substrate. This allows us to calculate the LiC_x and the Al_2O_3 dynamical response functions $\chi^0_{AC_x}$ and D_S separately, and then link them via Coulomb interaction, which saves the computational time tremendously.

In order to use these approximations, we need to verify their validity.

The validity of the RBA

The validity of the RBA can be checked by comparing the spectra calculated using the RBA with those obtained using the injected charge model (ICM) with the injected charge ΔQ_{TOT} chosen to cause the RBA Fermi level shift E_F. In the ICM we add extra charge to the unit cell, relax the unit cell and the atomic coordinates, calculate new KS wave functions and band structure and finally calculate the EELS.

We performed the ICM calculation for two characteristic RBA Fermi level shifts $E_F = -0.5$ eV and $E_F = 0.5$ eV. For the LiC_2 these shifts correspond to the extraction of 0.44 and the injection of 0.4 electrons per unit cell, respectively, while for the LiC_6 they correspond to the extraction of 0.77 and the injection of 1.06 electrons per unit cell, respectively. The characteristic parameters such as the injected charge ΔQ_{TOT}, the relative changes of the lattice constant $\Delta a/a$ and the change of the Li–C separation (with respect to the RBA) Δd are listed in Table 2. For LiC_2 we can see that the hole injection ($\Delta Q_{TOT} = -0.44$) weakly affects the crystal lattice, causing only a 0.1% increase of the unit cell, while the Li–C separation remains unchanged. On the other hand, the electron injection ($\Delta Q_{TOT} = 0.4$) causes a 2.4% increase of the unit cell, while the Li–C separation decreases for even 0.48 Å. The opposite happens for LiC_6, the hole injection ($\Delta Q_{TOT} = -0.77$) causes a −1.4% decrease of the unit cell, while the Li–C separation increases for 0.12 Å. The electron injection ($\Delta Q_{TOT} = 1.06$) causes a −0.1% decrease of the unit cell, and the Li–C separation almost does not change. Figure 7 shows comparisons of the EELS intensities calculated using the RBA (black solid) and the ICM (brown dashed), for two different wave-vector transfers and two different biases for each of the two systems, as described in the figure caption. Figure 7a shows the EELS intensity in LiC_2 for the hole injection $E_F = -0.5$ eV ($\Delta Q_{TOT} = -0.44$), and we can see that the spectra agree perfectly, as could be expected considering that for the hole injection the ICM crystal structure changes only negligibly. However, as can be seen in Fig. 7b, for the electron injection $E_F = 0.5$ eV ($\Delta Q_{TOT} = 0.4$) the spectra noticeably differ, i.e. the DP in the ICM spectrum is about 0.3 eV blue shifted. This is because the ICM Li–C separation decreases (with respect to the RBA one), the charge transfer from Li(σ) to C(π) band is larger, filling the Dirac cone and causing

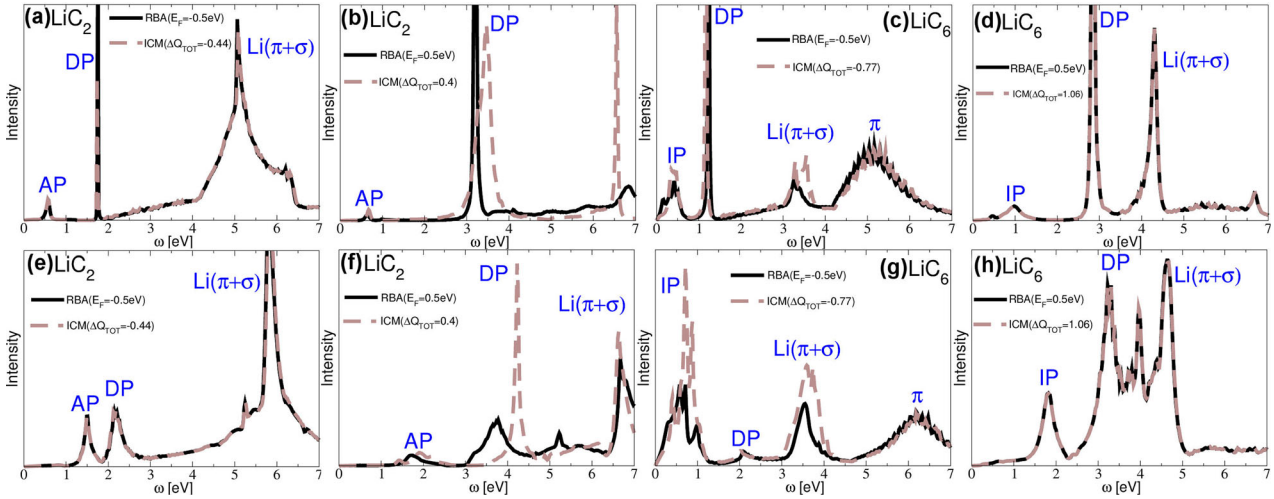

Fig. 7 Comparison between the EELS intensities in the LiC_2 and LiC_6 calculated using the rigid bands approximation (RBA) (black solid) and the injected charge model (ICM) (brown dashed). The RBA Fermi level shifts in LiC_2 are **a** $E_F = -0.5$ eV and **b** $E_F = 0.5$ eV, corresponding to the injection of $\Delta Q_{TOT} = -0.44$ and $\Delta Q_{TOT} = 0.4$ electrons per unit cell, respectively. The RBA Fermi level shifts in LiC_6 are **c** $E_F = -0.5$ eV and **d** $E_F = 0.5$ eV, corresponding to the injection of $\Delta Q_{TOT} = -0.77$ and $\Delta Q_{TOT} = 1.06$ electrons per unit cell, respectively. The transfer wave-vectors are $Q \approx 0.055$ .u. and $Q \approx 0.06$ a.u. for LiC_2 and LiC_6, respectively. The figures **e**–**h** show the same as the figures **a**–**d**, but the transfer wave-vector is $Q \approx 0.15$ a.u., for both systems.

the blue shift of the DP. Moreover, the DP obviously interacts more with different interband excitations and becomes broader. Also, the ICM spectrum shows a sharp peak at about 6.5 eV which does not exists in the RBA spectrum. Regardless of these differences the RBA and ICM spectra still qualitatively agree very well showing the most important features such as the weak AP, the strong DP and the Li($\pi + \sigma$) plasmon. The LiC_6 spectra show the opposite trend, i.e. the agreement is perfect for the electron injection (due to unchanged Li–C separation and only minor changes of the unit cell), as shown in Fig. 7d, while for the hole injection $E_F = -0.5$ eV ($\Delta Q_{TOT} = -0.77$), as shown in Fig. 7c the RBA and ICM spectra qualitatively agree very well, both spectra show the same features, a weak IP, a strong DP, and a Li($\pi + \sigma$) plasmon, but the ICM DP is now about 50 meV red shifted which is a consequence of the 0.12 Å increase of Li–C separation, which reduces the doping of the Dirac cone and hence reduces the DP frequency. Also the ICM IP and Li($\pi + \sigma$) plasmons are slightly more intensive. Figure 7e–h compare the RBA and ICM EELS intensities in LiC_2 and LiC_6 for the wave-vector transfer $Q \approx 0.15$ a.u., while the parameters ΔQ_{TOT} and E_F are the same as in Fig. 7a–d. We can notice the same behavior as for the smaller wave-vector transfers. For LiC_2 when the holes are injected, the RBM and ICM spectra coincide, but when the electrons are injected, the ICM DP is blue shifted, although this time it is a much sharper (narrower) mode than the RBA one. In addition to that, the ICM AP is slightly blue shifted. For LiC_6 the hole doping causes the ICM IP and Li($\pi + \sigma$) plasmon to be more intensive, while the weak DP is only slightly red shifted. For electron doping both spectra coincide showing important IP, DP, and Li($\pi + \sigma$) plasmons.

For larger hole ($E_F < -0.5$ eV) injections in LiC_2 and larger electron ($E_F > 0.5$ eV) injections in LiC_6, the RBA and ICM spectra remain in good agreement. However, for larger electron ($E_F > 0.5$ eV) injections in LiC_2 and larger hole ($E_F < -0.5$ eV) injections in LiC_6, the disagreement increases and the RBA can no longer be considered a reliable model. Finally, we can conclude that for $E_F \in [-0.5, 0.5]$ eV both ICM and RBA methods provide the most important plasmons such as AP, IP, DP, and Li($\pi + \sigma$), and that their energies and intensities agree qualitatively well (and in some cases even perfectly well). The RBA only affects the intensities of the IP, AP, DP, or Li($\pi + \sigma$) plasmons, and caused a small red or blue shift of the DP, but it does not contradict the interesting plasmonic phenomena which will be explained later. This definitely justifies the usage of the computationally much more efficient RBA method.

The validity of the van der Waals limit

In the van der Waals limit we assume that the LiC_x and Al_2O_3 surfaces interact only via the long-range fluctuation–fluctuation Coulomb interaction and that the individual LiC_x and Al_2O_3 orbitals and band structures remain unaffected. In order to verify the validity of this limit we compare the band structures of the self-standing LiC_x samples with the band structures of the LiC_x/Al_2O_3 composites. Special attention is paid to exploring how much the Al_2O_3(111) surface affects the parabolic Li(π) and Li(σ) bands, and the conical C(π) band, which are responsible for the formation of the AP, IP, DP, and Li($\pi + \sigma$) plasmons.

The crystal structure of the LiC_x/Al_2O_3 composites with minimal strain consist of huge supercells which exceed 200 atoms. Applying bias, to the system (via ICM) would require additional relaxation of the crystal structure, which would be computationally extremely difficult and the plausibility of the obtained result would be questionable. Therefore, we rather use smaller cells with larger strains, taking into account that this should not disturb the plausibility of the results of the band structure. The Al_2O_3 surface is modeled by three chemically compensated atomic layers O–Al–O obtained by cutting the bulk α-Al_2O_3 polymorph along the (111) plane. The crystal structure of the LiC_2/Al_2O_3 composite is then modeled so that the Al_2O_3(111) surface is biaxially strained by 2.4% in order to match the 2×2 graphene unit cell. The orientation of the LiC_2 crystal is chosen so that the Li atoms match the (111) hollow sites. The supercell obtained in this way consists of 20 atoms. The crystal structure of the LiC_6/Al_2O_3 composite is modeled in an equivalent way, only the Al_2O_3 is biaxially compressed by 11.3%, in order to match the graphene $\sqrt{3} \times \sqrt{3}$ unit cell. The supercell obtained this way consists of only 15 atoms. The orientation of the LiC_6 crystal is chosen so that the C atoms match the position of the topmost oxygen atoms. In both cases the separation between the topmost oxygen layer and the graphene layer is fixed to $h = 3.2$ Å. The ground state electronic densities are calculated using the $13 \times 13 \times 1$ K-point mesh sampling and the plane-wave cut-off energy is chosen to be 50 Ry. The crystal structures of the LiC_x/Al_2O_3 composites are sketched in Fig. 2 insets.

The arrows in Fig. 2a and b denote the inter-band transitions between the Li(σ) and Li(π) bands responsible for the occurrence of the Li($\pi + \sigma$) plasmon in the LiC_2, while the arrows in Fig. 2c, d denote the inter-band transitions between the Li(σ) and C(π) bands responsible for the occurrence of the inter-band inter-system IP plasmon in the LiC_6.

We can see that depositing the LiC_2 on the Al_2O_3(111) surface does not destroy the graphene C(π) cone and parabolic or the Li(σ) bands. The only difference is that the parabolic Li(σ) band is moved slightly down, by about 100 meV. On the other hand, we can see that the charge transfer into the graphene C(π) cone is negligible and the Dirac point remains ~−1.8 eV below the Fermi level. The effect of the substrate on the LiC_6 band structure is similar. The graphene C(π) and parabolic Li(σ) bands remain preserved. However, the Li(σ) band is shifted slightly up, by about 200 meV. Also the C(π) band is modified so that the gap at the Γ point slightly increases.

In conclusion, we can say that the relevant bands, the parabolic Li(π) and Li(σ) and the conical C(π) bands, are not changed significantly by the substrate, and that the modifications we mentioned are negligible and

cannot affect the plasmonic phenomena. This means that the van der Waals limit can be considered as fully justified.

DATA AVAILABILITY

The data generated during this study is available from the corresponding author on reasonable request.

CODE AVAILABILITY

The code used to produce the data presented in this study are available from the corresponding author on reasonable request.

Received: 16 September 2019; Accepted: 8 May 2020;
Published online: 06 July 2020

REFERENCES

1. Liao, L., Bai, J., Qu, Y., Huang, Y. & Duan, X. Top-gated graphene nanoribbon transistors with ultrathin high-*k* dielectrics. *Nanotechnology* **21**, 015705 (2010).
2. Yang, H. et al. An Al_2O_3 gating substrate for the greater performance of field effect transistors based on two-dimensional materials. *Nanomaterials* **7**, 286 (2017).
3. Niu, J., Shin, Y. J., Lee, Y., Ahn, J. H. & Yang, H. Graphene induced tunability of the surface plasmon resonance. *Appl. Phys. Lett.* **100**, 061116 (2012).
4. Fei, Z. et al. Edge and surface plasmons in graphene nanoribbons. *Nano Lett.* **15**, 8271 (2015).
5. Fanton, M. A. et al. Characterization of graphene films and transistors grown on sapphire by metal-free chemical vapor deposition. *ACS Nano* **5**, 8062 (2011).
6. Bonaccorso, F., Sun, Z., Hasan, T. & Ferrari, A. C. Graphene photonics and optoelectronics. *Nat. Photonics* **4**, 611 (2010).
7. Peng, Z., Yan, Z., Sun, Z. & Tour, J. M. Direct growth of bilayer graphene on SiO2 substrates by carbon diffusion through nickel. *ACS Nano* **5**, 8241 (2011).
8. Zhang, W. et al. Synthesize monolayer graphene on SiO_2/Si substrate with copper-vapor-assisted CVD method. *Mater. Res. Express* **5**, 125601 (2018).
9. Oliveira, M. H. Jr. et al. Formation of high-quality quasi-free-standing bilayer graphene on SiC (0001) by oxygen intercalation upon annealing in air. *Carbon* **52**, 83 (2013).
10. Politano, A. & Chiarello, G. Plasmon modes in graphene: status and prospect. *Nanoscale* **6**, 10927 (2014).
11. Koch, R. J. et al. Robust phonon–plasmon coupling in quasifreestanding graphene on silicon carbide. *Phys. Rev. Lett.* **116**, 106802 (2016).
12. Shin, S. Y. et al. Control of the π plasmon in a single layer graphene by charge doping. *Appl. Phys. Lett.* **99**, 082110 (2011).
13. Ismach, A. et al. Direct chemical vapor deposition of graphene on dielectric surfaces. *Nano Lett.* **10**, 1542 (2010).
14. Zhang, C. et al. Transfer-free growth of graphene on Al_2O_3 (0001) using a three-step method. *Carbon* **131**, 10 (2018).
15. Yang, G., Kim, H. Y., Jang, S. & Kim, J. Transfer-free growth of multilayer graphene using self-assembled monolayers. *ACS Appl. Mater Interfaces* **8**, 27115 (2016).
16. Kwak, J. et al. Near room-temperature synthesis of transfer-free graphene films. *Nat. Commun.* **3**, 645 (2012).
17. Hirano, R., Matsubara, K. & Kalita, G. Synthesis of transfer-free graphene on an insulating substrate using a solid phase reaction. *Nanoscale* **4**, 7791 (2012).
18. Fei, Z. et al. Infrared nanoscopy of Dirac plasmons at the graphene–SiO_2 interface. *Nano Lett.* **11**, 4701 (2011).
19. Low, T. & Avouris, P. Graphene plasmonics for terahertz to mid-infrared applications. *ACS Nano* **8**, 1086 (2014).
20. Yan, H. et al. Damping pathways of mid-infrared plasmons in graphene nanostructures. *Nat. Photonics* **7**, 394 (2013).
21. Pumera, M. Graphene in biosensing. *Mater. Today* **14**, 308 (2011).
22. Singh, E., Meyyappan, M. & Nalwa, H. S. Flexible graphene-based wearable gas and chemical sensors. *ACS Appl. Mater. Interfaces* **9**, 34544 (2017).
23. Mahmoudi, T., Wang, Y. & Hahn, Y.-B. Graphene and its derivatives for solar cells application. *Nano Energy* **47**, 51 (2018).
24. Miyoshi, Y. et al. High-speed and on-chip graphene blackbody emitters for optical communications by remote heat transfer. *Nat. Commun.* **9**, 1279 (2018).
25. Low, T. & Avouris, P. Graphene plasmonics for terahertz to mid-infrared applications. *ACS Nano* **8**, 1086 (2014).
26. Huang, S., Song, C., Zhang, G. & Yan, H. Graphene plasmonics: physics and potential applications. *Nanophotonics* **6**, 1191 (2017).
27. Jablan, M., Buljan, H. & Soljačić, M. Plasmonics in graphene at infrared frequencies. *Phys. Rev. B* **80**, 245435 (2009).
28. Novoselov, K. S., Falko, V. I., Colombo, L., Gellert, P. R., Schwab, M. G., Kim, K. A roadmap for graphene. *Nature* **490**, 192 (2012); Schwierz, F. Graphene transistors: status, prospects, and problems. *Proc. IEEE* **101**, 1567 (2013); Xia, F. The interaction of light and graphene: basics, devices, and applications. *Proc. IEEE* **101**, 1717 (2013).
29. Jablan, M., Soljačić, M. & Buljan, H. Plasmons in graphene: fundamental properties and potential applications. *Proc. IEEE* **101**, 1689 (2013).
30. Xiao, S., Zhu, X., Li, B.-H. & Mortensen, N. A. Graphene-plasmon polaritons: from fundamental properties to potential applications. *Front. Phys.* **11**, 117801 (2016).
31. Pervan, P. et al. Li adsorption versus graphene intercalation on Ir (111): from quenching to restoration of the Ir surface state. *Phys. Rev. B* **92**, 245415 (2015).
32. Halle, J., Neel, N. & Kroger, J. Filling the gap: Li-intercalated graphene on Ir (111). *Phys. Chem. C* **120**, 5067 (2016).
33. Petrović, M. et al. The mechanism of caesium intercalation of graphene. *Nat. Commun* **4**, 2772 (2013).
34. Tanaka, S. et al. Excitation of surface plasmons in highly-doped graphene by visible light (in the press).
35. Schumacher, S. et al. The backside of graphene: manipulating adsorption by intercalation. *Nano Lett.* **13**, 5013 (2013).
36. Cook, B., Russakoff, A. & Varga, K. Coverage dependent work function of graphene on a Cu (111) substrate with intercalated alkali metals. *Appl. Phys. Lett.* **106**, 211601 (2015).
37. Alattas, M. & Schwingenschlogl, U. Quasi-free standing graphene on Ni (111) by Cs intercalation. *Sci. Rep.* **6**, 26753 (2016).
38. Politano, A. et al. Evidence for acoustic-like plasmons on epitaxial graphene on Pt (111). *Phys. Rev. B* **84**, 033401 (2011).
39. Langer, T. et al. Sheet plasmons in modulated graphene on Ir (111). *New J. Phys.* **13**, 053006 (2011).
40. Politano, A., Marino, A. R. & Chiarello, G. Effects of a humid environment on the sheet plasmon resonance in epitaxial graphene. *Phys. Rev. B* **86**, 085420 (2012).
41. Politano, A., Yu, H. K., Farías, D. & Chiarello, G. Multiple acoustic surface plasmons in graphene/Cu (111) contacts. *Phys. Rev. B* **97**, 035414 (2018).
42. Ku-Ding, T., Plummer, E. W. & Feibelman, P. J. Surface-plasmon dispersion in simple metals. *Phys. Rev. Lett.* **63**, 2256 (1989).
43. Politano, A., Agostino, R. G., Colavita, E., Formoso, V. & Chiarello, G. Collective excitations in nanoscale thin alkali films: Na/Cu (111). *J. Nanosci. Nanotechnol.* **9**, 3932 (2009).
44. Politano, A., Formoso, V. & Chiarello, G. Electronic properties of metallic bilayers deposited on Cu (1 1 1): a comparative study. *Surf. Sci.* **603**, 933 (2009).
45. Chiarello, G. et al. Collective excitations of two layers of K on Ni (111). *Phys. Rev. B* **55**, 1376 (1997).
46. Despoja, V. et al. Strong acoustic plasmons in chemically doped graphene induced by a nearby metal surface. *Phys. Rev. B* **100**, 195401 (2019).
47. Marušić, L. & Despoja, V. Prediction of measurable two-dimensional plasmons in Li-intercalated graphene LiC_2. *Phys. Rev. B* **95**, 201408R (2017).
48. Despoja, V. & Marušić, L. UV-active plasmons in alkali and alkaline-earth intercalated graphene. *Phys. Rev. B* **97**, 205426 (2018).
49. Pitarke, J. M. et al. Theory of acoustic surface plasmons. *Phys. Rev. B* **70**, 205403 (2004).
50. Diaconescu, B. et al. Low-energy acoustic plasmons at metal surfaces. *Nature* **448**, 57 (2007).
51. Silkin, V. M. et al. Band structure effects on the Be (0001) acoustic surface plasmon energy dispersion. *Phys. Stat. Sol.* **205**, 1307 (2008).
52. Despoja, V., Novko, D., Lončarić, I., Golenić, N. & Silkin, V. M. Metal surface induces strong acoustic plasmons in chemically doped graphene. *Phys. Rev. B.* **100**, 195401 (2019).
53. Giannozzi, P. et al. QUANTUM ESPRESSO: a modular and open-source software project for quantum simulations of materials. *Matter* **21**, 395502 (2009).
54. Troullier, N. & Martins, J. L. Efficient pseudopotentials for plane-wave calculations. *Phys. Rev. B* **43**, 1993 (1991).
55. Perdew, J. P. & Zunger, A. Self-interaction correction to density-functional approximations for many-electron systems. *Phys. Rev. B* **23**, 5048 (1981).
56. Perdew, J. P., Burke, K. & Ernzerhof, M. Generalized gradient approximation made simple. *Phys. Rev. Lett.* **77**, 3865 (1996).
57. Monkhorst, H. J. & Pack, J. D. Special points for Brillouin-zone integrations. *Phys. Rev. B* **13**, 5188 (1976).
58. Saito, R., Dresselhaus, G. & Dresselhaus, M. S. *Physical Properties of Carbon Nanotubes* (Imperial College Press, London, 1998).
59. Novko, D. Dopant-induced plasmon decay in graphene. *Nano Lett.* **17**, 6991 (2017).

60. Despoja, V., Rukelj, Z. & Marušić, L. Ab initio study of electronic excitations and the dielectric function in molybdenum disulfide monolayer. *Phys. Rev. B* **94**, 165446 (2016).

ACKNOWLEDGEMENTS

V.D. acknowledges support from the QuantiXLie Center of Excellence, a project co-financed by the Croatian Government and European Union through the European Regional Development Fund—the Competitiveness and Cohesion Operational Program (Grant No. KK.01.1.1.01.0004). V.D. is also grateful to Donostia International Physics Center (DIPC) for hospitality during various stages of this work. Computational resources were provided by the DIPC Computing Center.

AUTHOR CONTRIBUTIONS

V.D. and L.M. proposed the studied systems and performed part of the EEL spectra calculations. J.J. contributed to the writing of the Introduction and performed EELS calculations in the ICM. N.G. performed the ground state crystal structure and band sctructure calculations of $LiC_x/Al_2O_3(111)$ composites. All authors discussed the results and contributed to the final manuscript.

COMPETING INTERESTS

The authors declare no competing interests.

ADDITIONAL INFORMATION

Correspondence and requests for materials should be addressed to V.D.

Reprints and permission information is available at http://www.nature.com/reprints

Publisher's note Springer Nature remains neutral with regard to jurisdictional claims in published maps and institutional affiliations.